

Structure control of 316L stainless steel through an additive manufacturing

Yu. O. Kuzminova^{†,1}, D. G. Firsov¹, S. D. Konev¹, A. A. Dudin², S. A. Dagesyan³,

I. Sh. Akhatov¹, S. A. Evlashin¹

[†]yulia.kuzminova@skoltech.ru

¹Center for Design, Manufacturing & Materials, Skolkovo Institute of Science and Technology, 30, bld.1, Bolshoy Bulvar, Moscow, 121205, Russia

²Institute of microelectronics and nanotechnology, RAS, 32A Leninsky Av., Moscow, 119991, Russia

³Department of Physics, M. V. Lomonosov Moscow State University, ½ Leninskie Gory, 119991 Moscow, Russia

The 3D printing process is a recent technique, which allows one to produce parts of complex geometry. The influence of printing parameters on the mechanical and structural properties of many materials has been extensively studied. However, despite the considerable amount of research, the task of comparing the results of different scientific groups is complicated. Each research group performs the investigation with different printing conditions. A lot of works contain not full information about the printing process parameters which were applied. This paper presents the results on the mechanical and structural properties of 316L stainless steel according to variable printing parameters, such as laser density energy, scan strategy, and build direction at other fixed conditions. The results reveal a parabolic dependency between the mechanical properties and the laser density energy. The laser density energy of 161 J/mm³ leads to the best mechanical characteristics (yield strength of 530 MPa, ultimate strength of 580 MPa, and ductility of 63.2%). Scan strategy does not influence the mechanical properties of the samples printed in the vertical direction. At the same time, the strong scan strategy effect is observed for the samples printed in horizontal direction. The difference in the ultimate strength between the vertically and horizontally printed samples reaches up to 70 MPa.

Keywords: powder bed fusion, additive manufacturing, stainless steel, mechanical properties, microstructure.

1. Introduction

Among different metal printing technologies, powder bed fusion (PBF) can be considered as the most promising. PBF technique allows printing parts with low porosity and high accuracy. This technology is being implemented into industrial production lines [1–4].

At the moment, there are many publications, which considered the impact of process parameters on the mechanical properties and structure of austenitic steel [5–11]. For instance, the “hatch angle” has an impact on the strength properties of stainless steel 304 [7]. Laser density energy [12,13] and chamber pressure [14] influence the porosity of the printing parts. Additionally, there are works which present controversial results for austenitic steel. Rotteger et al. [10] reported that fabrication of samples with strength in the vertical direction is higher than in the horizontal one, the ultimate tensile strength (UTS) is 522 MPa and 510 MPa, respectively. On the other hand, Tolosa et al. [8] found the highest strength properties in the horizontal direction, UTS=591 MPa in the vertical direction vs 685 MPa in the horizontal one. Debroy et al. [15] summarized the results of previous studies and did not reveal any dependency between the mechanical properties and the laser density energy.

A huge number of printing parameters does not allow to compare the results of individual studies. Moreover, not all works contain full information about the conditions of the printing process.

The present work considers the influence of the PBF printing parameters, such as build direction, laser density energy, and scan strategy on the structure and mechanical characteristics of printed 316L stainless steel. A comprehensive study on the influence of the printing parameters on structural and mechanical properties has been provided.

2. Material and methods

2.1. Material

Höganäs AB 316L stainless steel powder was used. The average size of the particles is 30 µm. The morphology and size distribution of the powder are presented in Fig. 1.

2.2. Manufacturing process

The PBF items were printed by a Trumpf TruPrint 1000 metal 3D printer (Germany) with a laser heat source. The printing process parameters were applied according to the manufacturer recommendations for 316L stainless steel, which are: laser power of 113 W, laser spot diameter of 55 µm, hatch spacing of 50 µm, layer thickness of 20 µm, scan strategy “chess x-y, 4 mm”, laser scan speed of 700 mm/s, gas (Ar) speed of 2.5 m/s, pressure in chamber of 1 bar, oxygen level of less than 0.3 at.%, no preheating of powder and build plate. Laser power, laser scan speed, and scan strategy were variable parameters.

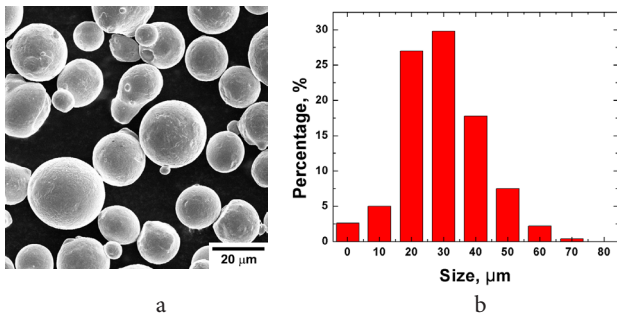


Fig. 1. SEM image (a) and size distribution (b) of powder 316L stainless steel particles.

The samples were divided into three groups according to variable parameters: laser density energy, printing strategy, and build direction.

2.3. Mechanical tests

Tensile testing according to ASTM E8/E8M-16a was conducted. Instron machine 5969 was used to test samples at speed of 10^{-3} s^{-1} . Digital Image Correlation system (Correlated Solutions, USA) was used for recording the specimen displacement during the test.

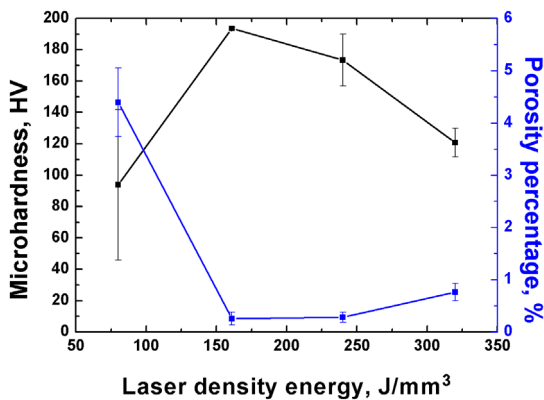
Microhardness was measured using a Nanovea PB 1000 with a load of 500 g for at least 6 measurements per point. The pyramid-shaped Berkovich cantilever was applied.

2.4. Structural analysis

Samples were cut for structural analysis. The top view surface was grounded with SiC abrasive paper (up to 2000 mesh) and polished with polishing suspensions (from 3 μm to 40 nm). For microscopic investigations, the samples were etched using a solution of 50 mL ethanol, 50 mL HCl and 2.5 g CuCl_2 .

Optical images were obtained with Carl Zeiss, Axio Scope.A1 (Germany) microscope. The porosity of the samples was analyzed with the Thixomet Pro software (Russia) according to ASTM E1245-03 standard.

Scanning electron microscopy (SEM), Carl Zeiss Supra 40 (Germany) was used to study structure of the samples. SEM microscope was equipped with an energy dispersive X-ray (EDX) detector to obtain the elemental characterization of the powder and the printed parts.



3. Results and discussion

3.1. Laser density energy

The first group of samples used laser density energy as a variable parameter, other parameters were fixed, the build direction was along the length of the samples. Laser density energy (LDE) was calculated for each case according to Eq. 1 [12]:

$$\text{LDE} = \frac{P}{h \times l \times V}, \quad (1)$$

where P — laser power (W), h — hatch spacing (mm), l — layer thickness (mm), V — laser scan speed (mm/s). Laser density energies of 80, 161, 240, and 320 J/mm^3 were applied, which correspond to 60 W & 750 mm/s, 113 W & 700 mm/s, 120 W & 500 mm/s, and 150 W & 470 mm/s laser power and laser speed, respectively.

Porosity decreases with LDE increasing up to 100 J/mm^3 [12]. At low energies, powder is not fully melted, thus leading to the formation of pores. Campanelli et al. [16] suggested that pores at a high laser density energy are formed due to the low melt element vaporization or due to the reaction between carbon and oxygen, which produce the spherical pores due to CO or CO_2 gaseous entrapment. Moreover, Taha et al. [17] suggested that the vaporization of moisture or oxides on the powder surface forms pores.

Additionally, Cherry [12] considered the correlation between the porosity value in a printed material and microhardness. In this work, we demonstrate the same dependence for porosity and laser density energy as in [12] (Fig. 2a). Fig. 3a confirms that the 80 J/mm^3 LDE is too low to melt the powder. Regions of unmelted powder are clearly observed. The lowest porosity is established for the LDE range of 161–240 J/mm^3 . Moreover, the impact of LDE is observed for the strength and ductility properties of the material, as well as microhardness (Fig. 2b). Table 1 summarizes the dependence of the mechanical properties on the laser density energy. The results of the mechanical properties are in good agreement with the analysis of microhardness and porosity. The best mechanical properties are achieved for $\text{LDE} = 161 \text{ J/mm}^3$.

SEM analysis revealed the presence of macro- and nanopores. The first type of pores is observed in optical images and has a different origin cause depending on the laser density energy. The presence of the second type of the pores

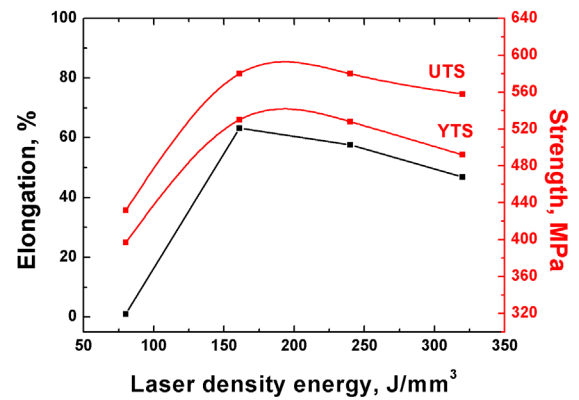


Fig. 2. (Color online) The laser density energy impact on microhardness and porosity value (a) and strength and elongation (b) of printed 316L stainless steel.

Table 1. The properties of the printed 316L stainless steel according to LDE.

LDE, J/mm ³	σ_y , MPa	σ_{UTS} , MPa	Elongation, %	Microhardness, HV	Porosity, %
80	397	432	1.0	93.8	4.39
161	530	580	63.2	193.6	0.25
240	528	580	57.6	173.3	0.28
320	492	558	46.8	120.7	0.76

does not depend on the laser density energy (Fig. 3 b and 3 c). Pores are formed by the element vaporization [16] and are mostly concentrated on the grain bordariers (Fig. 3 b).

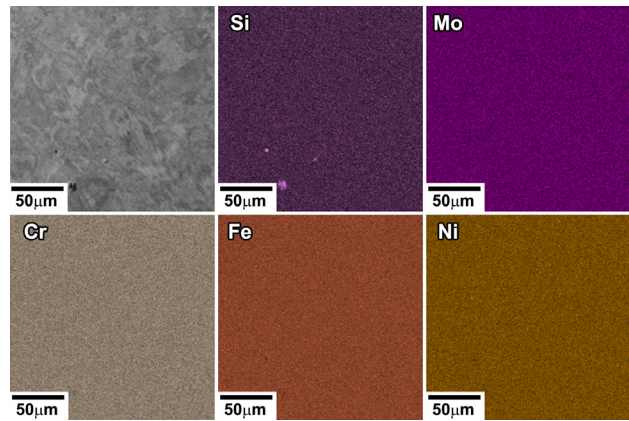
The formation of macropores at high LDE can be explained by the vaporization of the element with the lowest boiling point [16]. Mn is the element with the lowest boiling point in CoCrFeMnNi alloys, it has been demonstrated that Mn is being evaporated during the printing process [18]. According to the EDX results, macropores with a Si-rich surface can be observed (Fig. 4 a). The element composition does not change with increasing LDE (Fig. 4 b). A slight decrease in the element value is observed during the PBF process for such elements as Si and Cr. We can assume that the evaporation of Si and Cr during the printing process can explain the formation of both types of pores at high laser energies.

3.2. Scan strategy

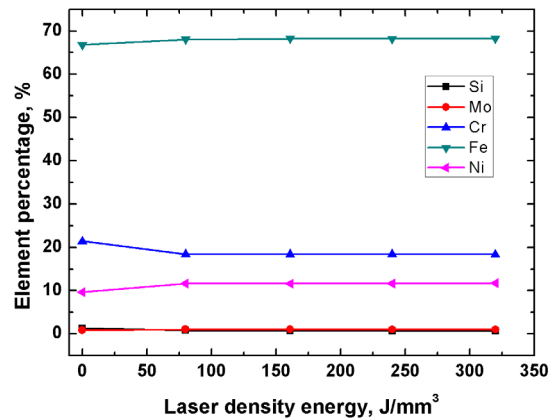
In this section the influence of the scan strategy as a variable parameter will be discussed, other parameters were fixed. The specimens were printed vertically. Optical images of structures for each scan strategy are presented in Fig. 5.

The “Chess” scan strategy fills the surface with squares of a specific side size. Samples with two square size values are considered, 1 and 4 mm. Each next layer is shifted relative to the previous one in a plane normal to the build direction. The “Line” scan strategy fills the surface with a laser track. Each next layer is turned through 90°. The “Strip” strategy fills the surface with strips of 2 mm width. Each next layer is turned through 45°. The “Offset” scan strategy fills the surface with circles from the center to the border.

The “Chess” scan strategy represents the melt pool boundaries with a width of 100 μm and axial directions (Fig. 5 Chess). The “Line” structure image represents overlapping of two layers with axial directions (Fig. 5 Line). It forms a regular



a



b

Fig. 4. (Color online) EDX maps for printing 316L stainless steel with LDE=161 J/mm³ (a); the element distribution for the printed 316L stainless steel (LDE=0 presents raw powder) (b).

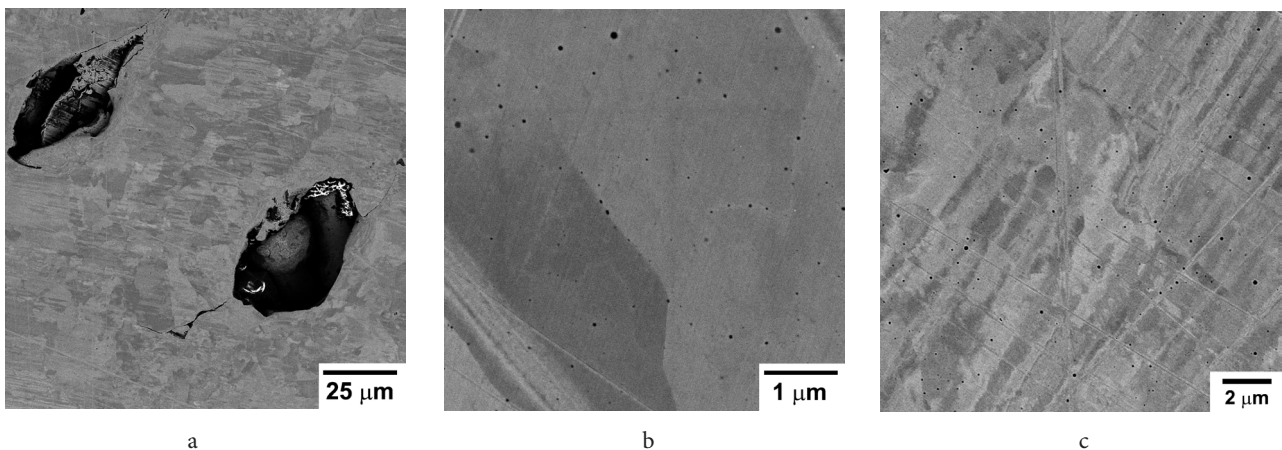


Fig. 3. The SEM images of as-printed 316L stainless steel with LDE of 80 (a), 161 (b), and 470 J/mm³ (c).

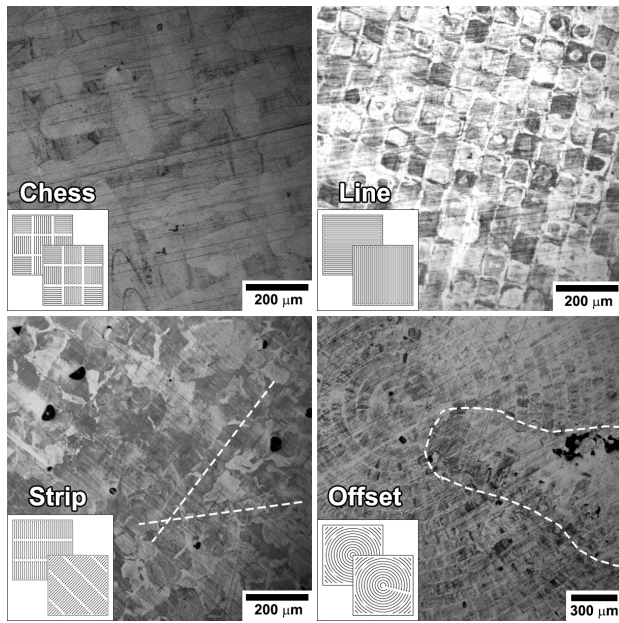


Fig. 5. The optical images of samples manufactured with different scan strategies.

square with side size of 75 μm. The “Strip” strategy represents the strip structural components with a width of 75 μm. An angle of 45° between the strips is observed in the Fig. 5 Strip. The printing process of “Offset” strategy was interrupted and deactivated. During the printing process, a balling effect appeared. A local increase of structural components can be observed in Fig. 5 Offset (dotted area).

Table 2 summarizes the results of mechanical tests and porosity analysis. The results of microhardness and porosity analysis are different for each scan strategy. The “Line” scan strategy demonstrates the highest microhardness value of 193.6 HV. This data correlates with the smallest porosity percentage of 0.07%. Martin et al. [19] demonstrated that the laser turn forms the major pores value. This explains the low porosity for the “Line” scan strategy. However, due to the ductile behavior of the material, the porosity value difference does not affect the mechanical properties. The strength and ductility characteristics are similar for all considered scan strategies.

3.3. Building direction

In this section, the effect of the transversal build direction is discussed. Three types of scan strategy were considered: 1) standard “Chess” 4 mm; 2) “Line along” the axis of the sample, and 3) “Line across” the axis of the sample.

The thermal gradient leads to the formation of an anisotropic structure. Previous works [7, 8, 10, 20] demonstrate the difference in mechanical properties for items printed in different directions. Herein, we demonstrate an increase in strength (by 30 MPa for yield tensile strength (YTS) and by 70 MPa for UTS) and decrease in ductility (by 33%) for samples printed in the horizontal direction (Fig. 6) which correlate with previous results [7, 8, 20]. Fig. 6 presents the structure in the plane of which the load was applied (Fig. 6 d provides the data from the vertically printed samples). The difference of mechanical properties for vertical and

Table 2. Results of mechanical and porosity analysis for 316L stainless steel.

Scan strategy	σ_y , MPa	σ_{UTS} , MPa	Elongation, %	Microhardness, HV	Porosity, %
Chess 4mm	530	580	63.2	193.6	0.25
Chess 1mm	521	575	69.6	180.3	0.87
Strip	524	565	69.2	151.8	0.56
Line	532	570	69.6	193.6	0.07

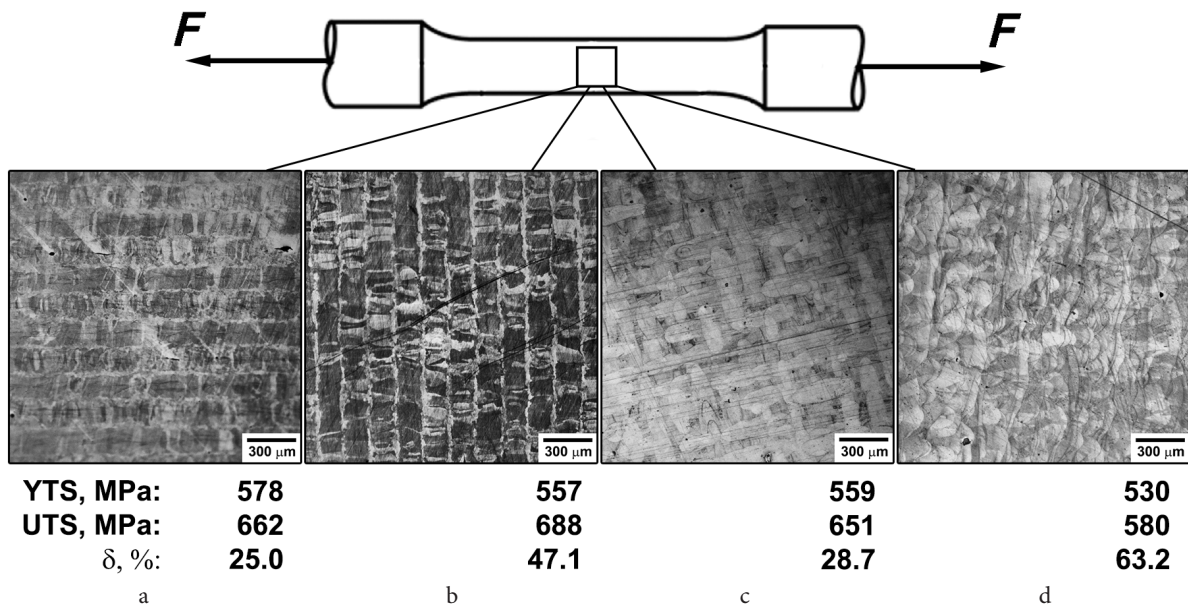


Fig. 6. The optical images of printed samples: “Line” strategy along (a) and across (b) the axis of the sample; “Chess” strategy top (c) and front (d) views, with mechanical properties for each scan strategy.

horizontal printed specimens is expected due to the anisotropic of microstructure formed by the melt pool boundaries.

Additionally, we compare the mechanical properties of samples printed in horizontal direction with different scan strategies. In that case, the scan strategy has a high impact on the mechanical characteristics. The “Line across” specimens have the highest strength properties (YTS of 557 MPa and UTS of 688 MPa) and highest ductility (47.1%) among samples printed in the horizontal direction, yet this value is lower than the ductility of vertically printed samples (63.2%). Fig. 6 presents the mechanical properties according to different structures of the material.

Fig. 7 presents SEM images of the front and top views of the “Chess” samples. The fine grained substructure caused by a high cooling rate [21] is visible for both views with grain size of 300 nm. In the front view, layers of 300 nm can also be observed (Fig. 7b). According to the Hall-Petch law, the high strength properties of AM materials are explained by the formation of fine grained structure [21].

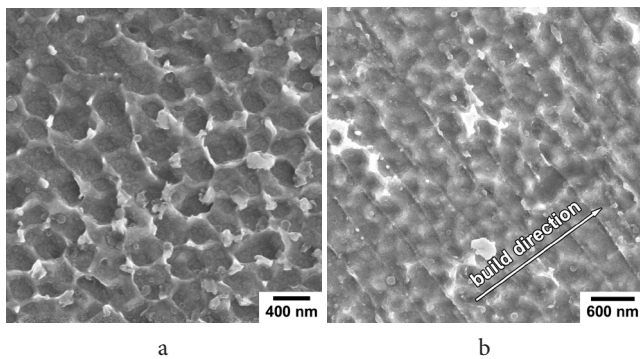


Fig. 7. SEM images of the structure top (a) and front (b) views of printed samples.

4. Conclusion

The present work considers the impact of printing parameters on the mechanical and structural properties of 316L stainless steel during the PBF process. According to obtained data, we can conclude that the laser density energy has a considerable impact on the material properties. Varying the laser density energy allowed to obtain samples with the lowest microporosity and mechanical characteristics of YTS=530 MPa, UTS=580 MPa, and δ =63.2%. The scan strategy does not have a significant effect on the mechanical properties of parts printed in the vertical direction. But the choice of the printing direction impacts the mechanical properties drastically; samples printed in the horizontal direction have YTS=559 MPa, UTS=651 MPa, and δ =28.7%. Moreover, for horizontally printed samples, the impact of the scan strategy on the mechanical properties is observed. Differences in mechanical properties can be achieved up to 48 MPa, 108 MPa, and 38.2% for yield strength, ultimate strength, and ductility, respectively.

References

1. J.O. Milewski. Springer series in materials science. Vol. 258. Cham, Springer (2017) 343 p. [Crossref](#)
2. W.E. Frazier. J. Mater. Eng. Perform. 23, 1917 (2014). [Crossref](#)
3. Z. Wally, W. van Grunsven, F. Claeysens, R. Goodall, G. Reilly. Metals. 6(5), 97 (2016). [Crossref](#)
4. H. Ali, H. Ghadbeigi, K. Mumtaz. Mater. Sci. Eng. A. 712, 175 (2018). [Crossref](#)
5. C. Pauzon, E. Hryha, P. Forêt, L. Nyborg. Mater. Des. 179, 107873 (2019). [Crossref](#)
6. A. Bin Anwar, Q.-C. Pham. J. Mater. Process. Technol. 240, 388 (2017). [Crossref](#)
7. K. Guan, Z. Wang, M. Gao, X. Li, X. Zeng. Mater. Des. 50, 581 (2013). [Crossref](#)
8. I. Tolosa, F. Garcíandía, F. Zubiri, F. Zapirain, A. Esnaola. Int. J. Adv. Manuf. Technol. 51, 639 (2010). [Crossref](#)
9. A. Simchi. Mater. Sci. Eng. A. 428, 148 (2006). [Crossref](#)
10. A. Röttger, K. Geenen, M. Windmann, F. Binner, W. Theisen. Mater. Sci. Eng. A. 678, 365 (2016). [Crossref](#)
11. E. Liverani, S. Toschi, L. Ceschini, A. Fortunato. J. Mater. Process. Technol. 249, 255 (2017). [Crossref](#)
12. J.A. Cherry, H.M. Davies, S. Mehmood, N.P. Lavery, S.G. R. Brown, J. Sienz. Int. J. Adv. Manuf. Technol. 76 (5–8), 869 (2015). [Crossref](#)
13. L. Hao, S. Dadbakhsh, O. Seaman, M. Felstead. J. Mater. Process. Technol. 209, 5793 (2009). [Crossref](#)
14. P. Bidare, I. Bitharas, R.M. Ward, M.M. Attallah, A.J. Moore. Int. J. Mach. Tools Manuf. 130–131, 65 (2018). [Crossref](#)
15. T. DebRoy, H.L. Wei, J.S. Zuback, T. Mukherjee, J.W. Elmer, J.O. Milewski, A.M. Beese, A. Wilson-Heid, A. De, W. Zhang. Prog. Mater. Sci. 92, 112 (2018). [Crossref](#)
16. S.L. Campanelli, N. Contuzzi, A. Angelastro, A.D. Ludovico. Capabilities and Performances of the Selective Laser Melting Process. In: New Trends in Technologies: Devices, Computer, Communication and Industrial Systems. (Ed. by M. J. Er). Rijeka, IntechOpen. (2010) pp. 233–252. [Crossref](#)
17. M.A. Taha, A.F. Yousef, K.A. Gany, H.A. Sabour. Materwiss. Werksttech. 43, 913 (2012). [Crossref](#)
18. R. Li, P. Niu, T. Yuan, P. Cao, C. Chen, K. Zhou. J. Alloys Compd. 746, 125 (2018). [Crossref](#)
19. A.A. Martin, N.P. Calta, S.A. Khairallah, J. Wang, P.J. Depond, A. Y. Fong, V. Thampy, G.M. Guss, A.M. Kiss, K.H. Stone, C.J. Tassone, J. Nelson Weker, M.F. Toney, T. van Buuren, M.J. Matthews. Nat. Commun. 10, 1 (2019). [Crossref](#)
20. H. Chae, E.-W. Huang, J. Jain, H. Wang, W. Woo, S.-W. Chen, S. Harjo, T. Kawasaki, S.Y. Lee. Mater. Sci. Eng. A. 762, 138065 (2019). [Crossref](#)
21. D. Herzog, V. Seyda, E. Wycisk, C. Emmelmann. Acta Mater. 117, 371 (2016). [Crossref](#)